006
EXPERIMENTAL TESTS AND CFD SIMULATIONS ON A TILTWING AIRCRAFT IN HOVER

G. Droandi*, G. Gibertini*, D. Grassi*, G. Campanardi*, A. Zanotti*

*Dipartimento di Scienze e Tecnologie Aerospaziali – Politecnico di Milano
Campus Bovisa, Via La Masa 34, 20156 Milano – Italy
e–mail: giovanni.droandi@polimi.it

Keywords: Tiltrotor, Tiltwing, Aerodynamic, Rotor, Experimental model, PIV measurements, CFD calculations.

Abstract

In the present work, the aerodynamic interaction between the rotor wake and the wing on a high–performance tiltwing aircraft operating in hover has been investigated. Both experimental and numerical approaches have been used to give a detailed description of the main physical phenomena related to this problem. The performance of the aircraft and the flow field between the wing and its rotor have been analysed making use of force and PIV (Particle Image Velocimetry) measurement techniques. High accuracy numerical simulations have been carried out by means of an in–house CFD (Computational Fluid Dynamics) code and both steady and time accurate calculations have been performed on the aircraft titled wing configuration. Numerical predictions have been validated by comparing the simulation results with experimental data and have been used to help the description of the flow field around the aircraft.

Nomenclature

A	=	Rotor disk area, πR^2
β	=	Blade flap angle
c^b	=	Blade chord
c^w	=	Wing chord
C_P	=	Power coefficient, $P/(\rho A\Omega^3 R^3)$
C_T	=	Thrust coefficient, $T/(\rho A\Omega^2 R^2)$
FM	=	Figure of merit, $C_T^{3/2}/(C_P\sqrt{2})$
F_x^w	=	Wing x–force component
F_z^w	=	Wing z–force component
F_z^r	=	Rotor z–force component
h^w	=	Wing rotation axis and rotor disk distance
M_{Tip}	=	Blade tip Mach number
n	=	Rotor rotational speed
N_b	=	Rotor number of blades
Ω	=	Rotor angular speed
P	=	Rotor power
ψ	=	Azimuthal angle position
R	=	Rotor radius
σ	=	Rotor solidity, $c^b N_b/(\pi R)$
U_z	=	Z–velocity component
U_x	=	X–velocity component
T	=	Rotor thrust
τ	=	Wing tilt angle
θ	=	Collective pitch angle
ρ	=	Air density
ξ	=	Blade led–lag angle

1 Introduction

After about 50 years of research, tiltrotor aircraft are today a reality in the modern rotorcraft scenario combining together the advantages and the peculiarities of helicopters with modern propeller aircraft and representing a concrete possibility to overcome the main limitations of both of them [1]. Thanks to their high versatility, tiltrotor aircraft represent nowadays a very attractive compromise for the civil industry [2]. However, some important limitations are still present in conventional tiltrotor design. For instance, in helicopter mode the aerodynamic interaction that occurs between the wing and the rotors is responsible for loss of rotor performance [3] and negatively affects the hovering performance and the lifting capability of the aircraft. With the aim of overpassing these limitations, non–conventional tiltrotor configurations have been investigated during last years. An interesting and promising solution, the tiltwing concept, has been proposed in the frame of the project ERICA (Enhanced Rotorcraft Innovative Concept Achievement [4]) founded by the European Community at the beginning of 2000s. As known, a tiltwing aircraft has the possibility to tilt the external part of the wing with the rotor minimising the wing surface on which the rotor wake strikes and preserving good hover performance [5], [6]. Even if the ERICA tiltrotor was the subject of several experimental and numerical studies during the last 14 years [7], [8], [9] many aspects of this configuration, have to be further analysed for possible future evolutions and applications.

In the present work, the aerodynamic interaction between wing and rotor on a high–performance tiltwing aircraft in hover has been investigated. For this purpose, both experimental and numerical approaches have been used to give a detailed description of the main physical phenomena related to the interaction between wing and rotor in this kind of aircraft. A tiltwing aircraft in the same class of ERICA has been used for this study. The reference full–scale aircraft geometry was characterised by a wing span of 15 m and two rotor with a radius of 3.7 m (for further details on the reference configuration see [5]). In order to study the hovering flight condition and the first part of the conversion corridor, a 1/4 scaled wind tunnel half–model [6] has been designed and manufactured at POLIMI (Politecnico di Milano).

The performance of the aircraft and the flow field between the wing and its rotor have been analysed making use of different experimental techniques. Since force measurements may give only partial information about the phenomena related to the aerodynamic interaction between wing and rotor, PIV (Particle Image Velocimetry) measurements have been carried out on some interesting planes around the model [10]. Since in hover the interaction between the rotor and the wing is very complex, numerical simulations have been used to help the description of the flow field around the aircraft. In this regards, high accuracy calculations have been carried out by means of an in–house CFD (Computational Fluid Dynamics) code. Once numerical predictions have been validated by comparing the simulation results with experimental data, numerical calculations have been used to get a detailed insight in the main phenomena associated with aerodynamic interference between wing and rotor.

2 Experimental test rig

An experimental test rig representing one half–wing together with the corresponding rotor and nacelle has been designed for hovering tests and has been realised in the DSTA (Dipartimento di Scienze e Tecnologie Aerospaziali) Aerodynamics Laboratory of POLIMI. In the present section, the 0.25 scaled tiltwing half–model is presented and a detailed description of the measurement system is given.

2.1 Tiltwing half–model

In order to design the wind tunnel model [11] a geometrical scale of 1/4 with respect to the full–scale aircraft was selected. The experimental test rig consisted of two main independent subsystems: the rotor system and the half–wing with an image plane. These two main systems were not linked in any parts in order to measure

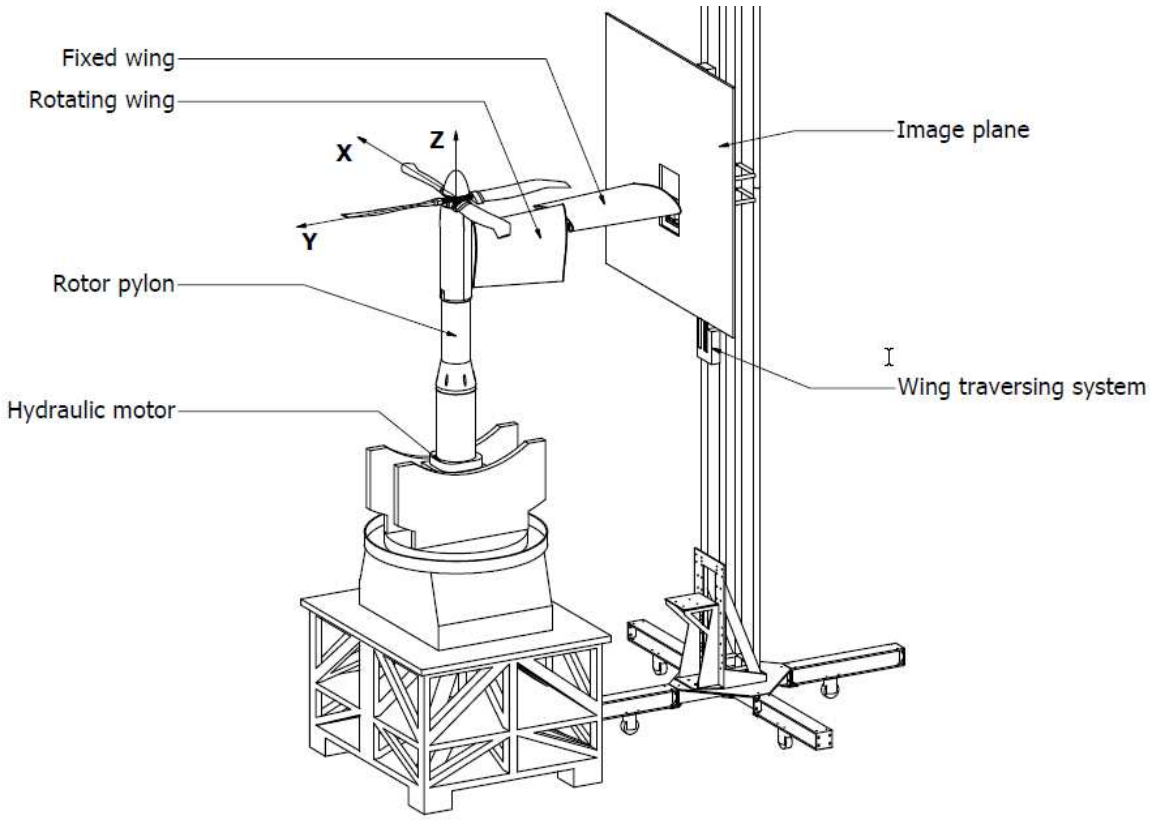

Figure 1: Schematic view of the experimental test rig and model reference system.

the rotor and the wing loads separately and to test both the isolated rotor and the aircraft half–model configurations. The test rig components and the model reference system are shown in Figure 1. The origin of the model reference system is located on the rotor hub, at the intersection point between the rotor axis and the rotor disk. The z axis lies on the rotor axis and points upward, the y axis is parallel to the wing axis and goes from the aircraft symmetry plane to the rotor, and the x axis is defined following the right hand side rule.

The rotor was powered by a hydraulic motor (maximum power 16 kW at 3000 rpm) located inside a swivelling basement which is placed on an aluminium base. The rotor hub was mounted on a rigid pylon composed by three main parts and located over the hydraulic motor. The first part of the rotor pylon is directly fixed on the motor and the transmission shaft passes through it. Inside the second portion of the pylon, a 24–channel slip ring is located over the transmission shaft (with a diameter of 35 mm) for the transmission of electrical power and signals from and to the rotating part of the rotor hub. A Hall Effect Sensor positioned on the same shaft was employed to measure the rotational speed of the rotor. The rotor hub is located in the third part of the rotor pylon that includes instruments to measure the loads acting on the system. The rotor had four blades designed in–house by means of a multi–objective genetic optimisation procedure (for further details see [12]). The experimental rotor model had a radius of $R = 0.925$ m and it was placed at a height of 5 R from the ground. During the experimental tests, the nominal rotational speed of the rotor, which rotates in the anti–clockwise direction, was $n = 1120$ rpm. The tip Mach number was 0.32 which correspond to 1/2 the tip Mach number of full–scale aircraft at design point in hover. The thrust given by the rotor has been measured by a holed six–component strain gauge balance located under the rotor hub. The torque has been measured by an in–house instrumented holed shaft which passed through the balance and it was directly linked to the rotor hub shaft by a motoring coupling. Under the instrumented shaft, a flexible joint was employed to avoid the transfer of axial force to the lower part of the transmission shaft providing also compensation for axial, angular and radial misalignments [11]. The carbon fibre nacelle, manufactured in–house, had an external maximum diameter of 0.27 R and it was not weighted because it was mounted on the lower part of the rotor pylon. Since the nacelle air intake was not taken into account in this study it was not present on the nacelle model. A picture of the test ring in the open test section of the POLIMI wind tunnel is shown in Figure 2.

The collective, longitudinal and lateral pitch controls were provided to the blades by means of three indepen-

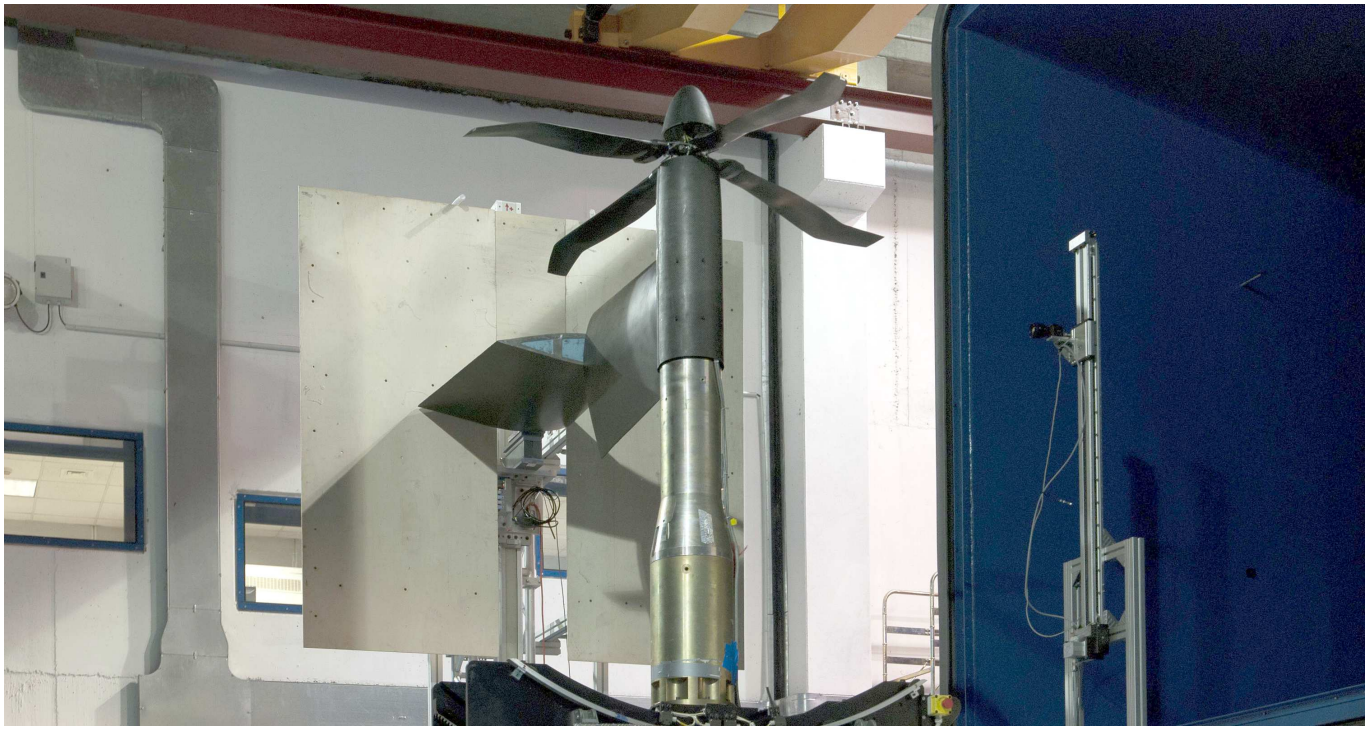

Figure 2: The test rig in the POLIMI Wind Tunnel.

dent electric actuators acting on the swashplate. Each blade was attached to the rotor hub through the flap, led–lag and pitch hinges located in different positions. The led–lag hinge was located beyond the flap hinge while the feathering bearing was placed further outboard. In the present case, no dampers were fitted on the led–lag hinge of the rotor model. In details, the flap hinge had an offset of $e_f = 3.2$ % of the rotor radius while the lag hinge had an offset of $e_{ll} = 5.4$ %. In order to change the position of the blade, the blade cuff could be rotated around the feathering axis by means of the pitch horn that was attached to the blade cuff outboard of the pitch bearing. The connection between the pitch horn and the pitch link laid on the flap hinge axis assuring no pitch–flap coupling. Each blade hinge was instrumented with a high accuracy Hall effect sensor and Alnico magnet to directly measure the pitch (θ, positive nose up), led–lag (ξ, negative ahead) and flap (β, positive upwards) angles on the rotor hinges.

The half–wing model had a span of 1.90 R and it has to be intended as the distance from the aircraft symmetry plane (wing root, $c^w = 0.810\ R$) to the nacelle junction (wing tip, $c^w = 0.562\ R$). The internal structure of both wing portions was composed by Styrofoam (extruded polystyrene foam) while aluminium formers were placed at the extremities of each part. The external skin of the wing was made by a 2–layers carbon fibre skin. The tilt section was ($c^w = 0.676\ R$) located 1.01 R from the symmetry plane and the external part of the wing could rotate from $\tau = 0°$ (untilted configuration) to $\tau = 90°$ (tilted configuration). The wing was linearly tapered, untwisted and all sections were aligned with respect to 25 % of the local chord. The design distance between the wing rotation axis and the rotor disk was $h^w = 0.465\ R$. All the wing sections employed a NACA 64A221 [13], [14]. The wing was mounted on an independent traversing system and was not connected to the nacelle and rotor in order to have a more accurate evaluation of the effects due to the impingement of the rotor wake on the airframe model. Forces and moments on the wing were measured by a seven–component strain gauge balance located at the wing root. In order to restore the symmetry condition on the symmetry plane of the model, an image plane was placed at the fixed wing root ad was fixed on the support of the wing traversing system. The image plane was 2.2 R high and 2.2 R wide [15], [16].

2.2 PIV set up

The flow physics of the phenomena related to the aerodynamic interaction between the rotor wake and the wing in a tiltwing aircraft is complex and completely unsteady. Due to this, the PIV technique has been involved to get an in-depth examination of the rotor wake behaviour. An extensive 2C PIV campaign has been carried out for both the isolated rotor and the half-model with the tilted wing. The PIV setup [17] was composed by a Nd:YAG double pulsed laser with 200 mJ output energy and a wavelength of 532 nm and a double

shutter CCD camera with a 12 *bit*, 1952 $\times$ 1112 pixel array. The laser was alternatively mounted below the rotor disk and in front of the tilted wing to light respectively a plane at x–constant and a plane at y–constant. The plane at x–constant considered for the tiltwing half–model configuration was shifted by $x = -0.079\ R$ (see Figure 3(b)b) with respect to the isolated rotor test case (see Figure 3(a)a) in order to avoid the interference of the light sheet with the tilted wing. The camera was located on a single axis traversing system to move the measurement window in vertical direction. The PIV measurement area on the x-constant plane was 0.38 R wide and 0.90 R high for the isolated rotor while it was 0.38 R wide and 0.63 R high for the half-model configuration. The outer edge of the measurement area is aligned with the tilt-wing section while the upper edge is located at $z = 0.15\ R$. y-constant planes at $y/R = -0.69$ and $y/R = -0.79$ were surveyed only for the half-model configuration to evaluate the swirl in the rotor wake flow over the leading edge of the tilted wing. For this test case, the PIV measurement area was 0.27 R wide and 0.30 R high. In order to achieve better resolution of the image pairs, the measurement area was composed by four adjacent windows for the isolated rotor case while it was composed by three adjacent windows for both x-constant and y-constant planes for the half-model configuration. The adjacent windows had small overlapping band between them. Phase-locked PIV measurements were carried out by synchronising the laser pulses with a prescribed azimuthal position of a selected rotor blade. The synchronisation of the PIV instrumentation was controlled by a 6 channels pulse generator while a particle generator with Laskin atomiser nozzles was used for the seeding. The image pairs were post–processed by using the PIVview 2C software [18] developed by PIVTEC. Multigrid technique [19] was employed to correlate the image pairs, up to an interrogation window of 32 $\times$ 32 pixels.

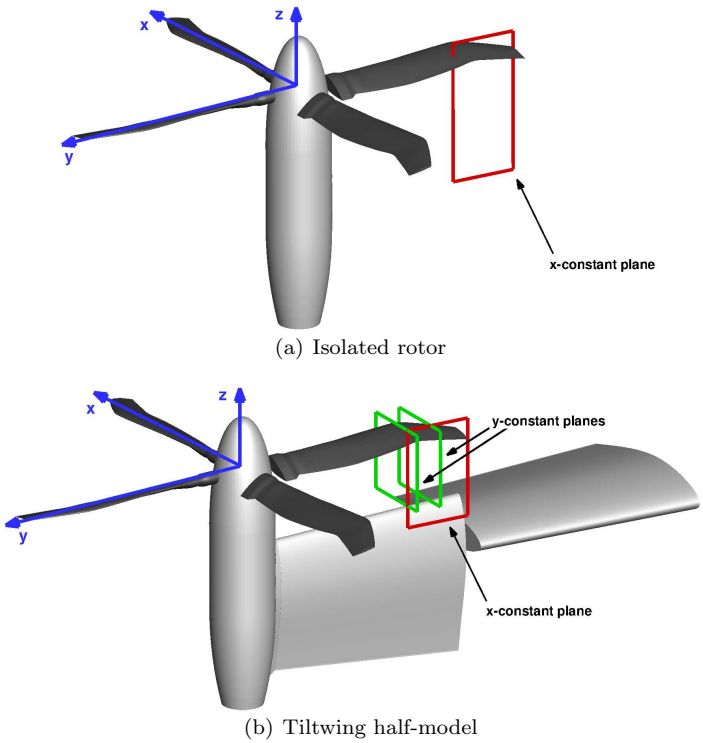

(a) Isolated rotor

(b) Tiltwing half-model

Figure 3: Schematic view of the PIV measurement planes.

3 Numerical calculations

The study of the aerodynamic interaction on a tiltwing aircraft operating in hover was the main objective of the experimental campaigns carried out in the DSTA Aerodynamics Laboratory. Due to the high complexity of the problem, a numerical activity was done in parallel to the experimental tests in order to get more information about the physics of the phenomena due to the aerodynamic interaction between the wing and the rotor wake.

3.1 Flow solver ROSITA

The CFD code ROSITA (ROtorcraft Software ITAly) [20] numerically integrates the unsteady Reynolds Averaged Navier–Stokes Equations (RANS) equations, coupled with the one–equation turbulence model of Spalart–Allmaras [21]. Multiple moving multi–block grids can be used to form an overset grid system by means of the Chimera technique, as described in the following. To simplify the solution of the flow field in overset grid systems, the Navier–Stokes equations are formulated in terms of the absolute velocity, expressed in a relative frame of reference linked to each component grid. The equations are discretised in space by means of a cell–centred finite–volume implementation of the Roe's scheme [22]. Second order accuracy is obtained through the use of MUSCL extrapolation supplemented with a modified version of the Van Albada limiter introduced by Venkatakrishnan [23]. The viscous terms are computed by the application of the Gauss theorem and using a cell–centred discretisation scheme. Time advancement is carried out with a dual–time formulation [24], employing a 2^{nd} order backward differentiation formula to approximate the time derivative and a fully unfactored implicit scheme in pseudo–time. The equation for the state vector in pseudo–time is non–linear and is solved by sub–iterations [25]. In the dual–time method, there is no stability limit with respect to the size of the physical time step Δt and this approach can lead to a large reduction in CPU time compared to a fully implicit method in physical time. The physical time step Δt is here only limited by solution accuracy requirements. However, there is a stability condition on the

pseudo–time step, as shown by Hirsch [26] for viscous flow calculations. The generalised conjugate gradient (GCG), in conjunction with a block incomplete lower–upper preconditioner, is used to solve the resulting linear system.

The connectivity between the (possibly moving) component grids is computed by means of the Chimera technique. The approach adopted in ROSITA is derived from that originally proposed by Chesshire and Henshaw [27], with modifications to further improve robustness and performance. The domain boundaries with solid wall conditions are firstly identified and all points in overlapping grids that fall close to these boundaries are marked as holes (seed points). Then, an iterative algorithm identifies the donor and fringe points and lets the hole points grow from the seeds until they entirely fill the regions outside the computational domain. To speed up the search of donor points, oct-tree and alternating digital tree (ADT) data structures are employed.

The ROSITA solver is fully capable of running in parallel on computing clusters. The parallel algorithm is based on the message passing programming paradigm and the parallelisation strategy consists in distributing the grid blocks among the available processors. Each grid block can be automatically subdivided into smaller blocks by the solver to attain an optimal load balancing.

Numerical computations have been carried out alternatively on two different clusters. The first one is the Lagrange cluster at CINECA, made up of 208 bi-processor Intel® Xeon QuadCore 3.166 GHz nodes interconnected by an Infiniband $4X$ Double Data Rate with capacity of 20 Gb/s. The second one is the Eurora cluster at CINECA, made up of 32 bi–processor eight–core Intel® Xeon® CPU E5–2658 at 2.10 GHz with 16 GB RAM and 32 bi–processor eight–core Intel® Xeon® CPU E5–2687 at 3.10 GHz with 16 GB RAM interconnected by a Qlogic QDR Infiniband high–performance network with capacity of 40 Gb/s. Numerical activities on the latter cluster has been carried out in the frame of the project ISCRA named IscrC_ASTRO.

3.2 Numerical models

Numerical calculations with the CFD code ROSITA were run following two different approach with increasing complexity to model the rotor. The only flight condition considered in the numerical activity is the hover condition with the wing placed at the design distance from the rotor disk ($h^w = 0.465\ R$) and with the external part of it tilted ($\tau = 90°$). A steady–state approach was used in order to get information about the mean aerodynamic loads acting on the wing, while a time accurate approach was employed to investigate both the rotor and wing loads variation in time. In the first case, and actuator disk model was used to represent the rotor loads instead of simulating the flow around rotating blades. Since the steady–state assumption gives a strong reduction of computational times with respect to the unsteady approach, steady calculations were used to numerically evaluate the effects of the rotor wake on the wing at several C_T/σ corresponding to some exper-

Trim condition	C_T/σ	θ [deg]
TC1	0.007	2
TC2	0.018	4
TC3	0.031	6
TC4	0.061	8
TC5	0.076	10
TC6	0.096	12
TC7	0.113	14

Table 1: Rotor trim conditions for steady calculations. Data taken from steady isolated rotor simulations in hover (see [11]).

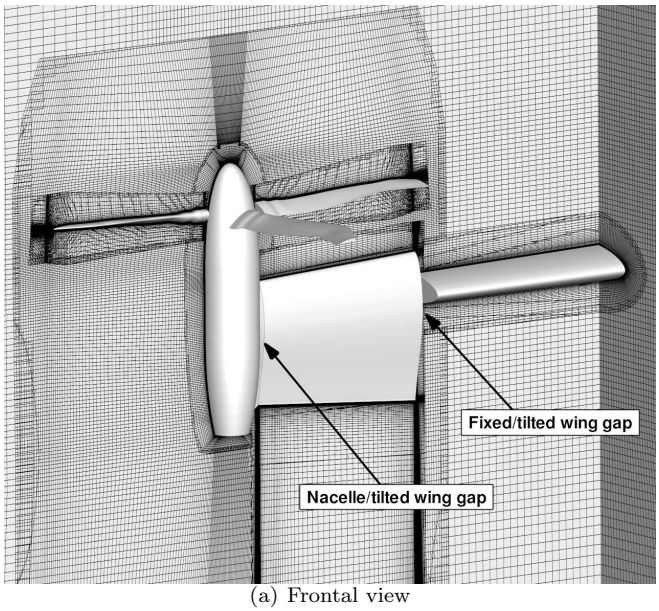

(a) Frontal view

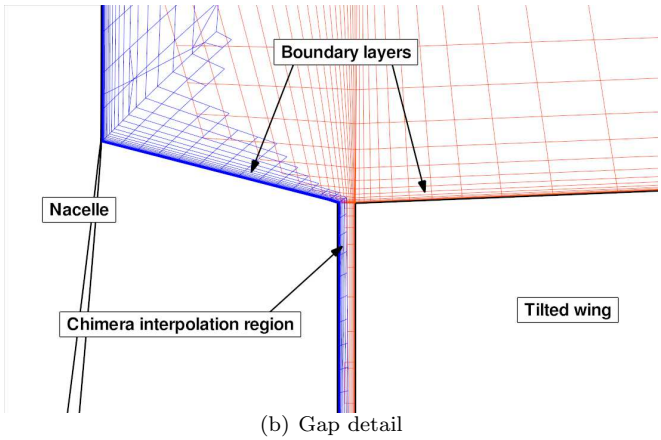

(b) Gap detail

Figure 4: Details of grids system for CFD calculations.

Grids	No. Blocks	No. Cells ($\times 10^6$)	No. Blocks	No. Cells ($\times 10^6$)
Farfield 1	5	0.629	5	0.629
Farfield 2	6	1.451	6	1.451
Nacelle	6	2.803	6	2.803
Nacelle inter.	4	3.113	4	3.113
Wing 1	6	1.816	6	1.816
Wing 2	9	2.185	9	2.185
Actuator Disk	1	0.290		
Blade			8 ($\times 4$)	1.813 ($\times 4$)
Total	37	12.287	68	19.249

Table 2: Computational mesh details for half–aircraft calculations.

imental tests conditions, as reported in Table 1. However, since the flow field in which the wing is immersed is completely unsteady, steady computations allow to resolve only the mean loads developing on the wing giving no information on the loads time dependency. Moreover, steady simulations cannot take into account the effects that the wing has on the rotor loads. For these reasons, a time accurate simulation was carried out for the trim condition TC6 of the rotor (this condition is the same used for the PIV surveys) to analyse the phenomena related to the unsteady nature of the rotor/wing aerodynamic interaction.

Due to the high complexity of the problem geometry, cartesian multi–block grids were used to represent the flow field around bodies and the Chimera method was employed to simplify the mesh generation process. Moreover, the Chimera method allows to build a set of grids that can be used to run alternatively steady and unsteady simulations by changing only the actuator disk grid with four equal grids describing the rotating blades. Since unsteady calculations are much more time consuming than steady ones, the grids were designed to obtain a final computational mesh with a certain amount of elements which represents a good compromise between the quality of the mesh and the computational cost of each run. With the aim to limit the total number of cells, the background mesh was composed by 2 different cartesian multi–block grids, one fine (the inner grid, Farfield 1) and one coarse (the outer grid, Farfield 2). All the other grids were contained inside the finest background grid, having similar spatial resolution at the outer edges, as shown in Figure 4(a). Both wings were meshed in a C–H topology while the nacelle was meshed in a O topology. In general, the bodies' grids were generated to have high mesh quality close to the bodies' surfaces and limited spatial extension around them. A critical feature of the grid generation process was represented by the gaps involved between the two wings and between the outer wing and the nacelle. Since in the experimental model both gaps were in the order of 0.001 m, to guarantee a sufficient overlap region for the Chimera tagging procedure, the bodies' grids have been modelled with particular care in those regions. A detail of the gap between the tilted wing and the nacelle is shown in Figure 4(b). The wings had the outer boundaries located 0.2 R away from their surfaces except in the wake direction where the boundaries were located 1.4 R from the trailing edge. The outer boundary of the nacelle grid was located 0.2 R away from its surface in all directions. The nacelle grid and the outer wing grid were contained inside an intermediate cylindrical grid (with a radius of 1.3 R) that was generated to better capture the rotor wake given by the actuator disk or by the rotating blades. The details of each grid are reported in Table 2. Since the root of the fixed wing (wing 1) lied on the aircraft symmetry plane, a symmetry condition has been applied to that plane, whereas both wings and the nacelle surfaces have been modelled through no–slip boundary conditions.

In the steady–state approach, simulations have been carried out by reproducing the effects of the rotor with an actuator disk. The actuator disk model embedded in ROSITA approximates the forces applied by the rotor blades to the air flow over a disk having the same diameter of the rotor. The actuator disk grid models a disk without thickness in a single layer of cells of a cylindrical O–H grid in which a non uniform source distribution is given to reproduce the desired force (per unit area) distribution [28]. A view of the grid system employed for the steady computations is reported in Figure 6. The disk without thickness has been placed on the tip path plane of the rotor. Since this plane is defined by the rotor trim condition, the spatial location of the disk changed for every $C_T\sigma$ analysed. The force distribution on the disk has been computed from knowledge of the load distributions on the blades (two examples of loads distributions are shown in Figure 5, [6], [11]).

The time accurate simulation has been carried out on a final grid with a total number of cells higher than the one adopted for the steady calculations (see Table 2). As previously mentioned, the computational mesh for the unsteady simulation has been obtained by replacing the actuator disk grid with four identical grids. Each grid was composed by 1.813×10^6 cells and contained one blade. A C–O grid meshing topology has been used to ensure a very good nodes distribution and orthogonality

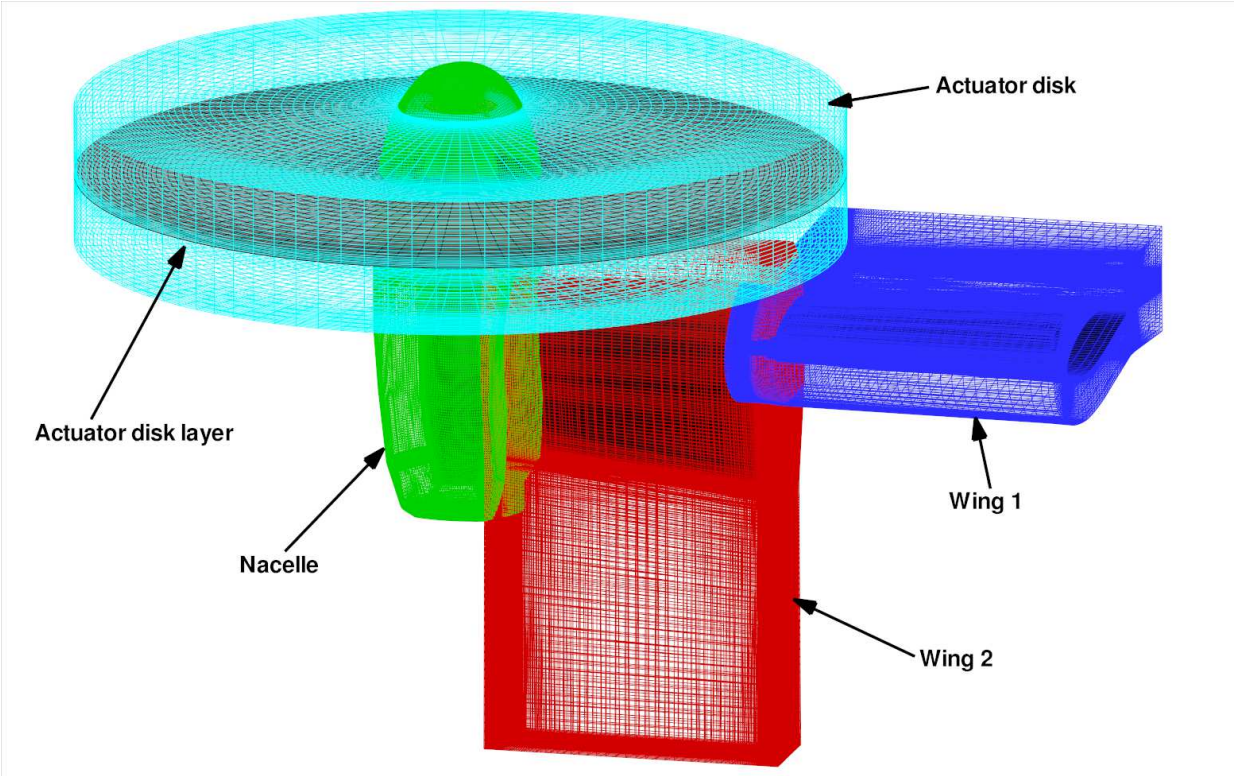

Figure 6: View of bodies' grids system for steady CFD calculations.

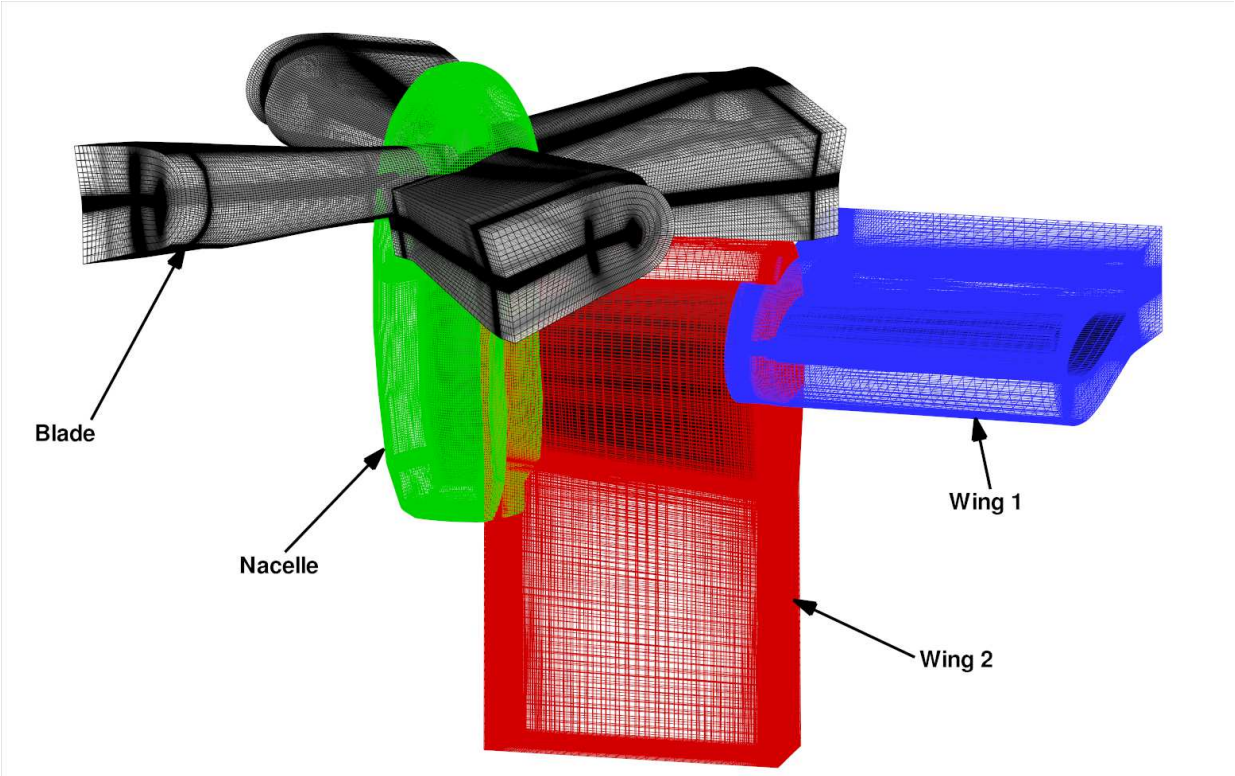

Figure 7: View of bodies' grids for unsteady CFD calculation.

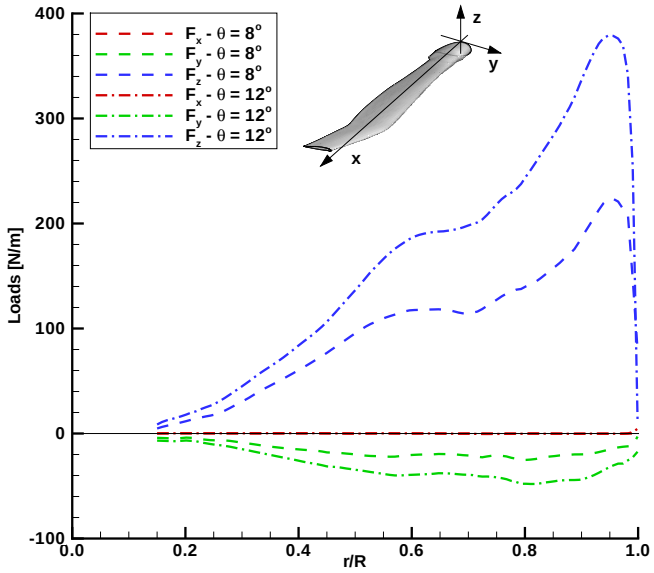

Figure 5: Example of load distributions on a single blade for TC4 and TC6.

in the proximity of the blade surface. A view of the grid system used for the unsteady simulation is reported in Figure 7. The blade has been fairly well discretised in terms of nodes distribution along the chord and the normal surface directions (a hyperbolic law has been adopted in both directions), but also in the span–wise direction, especially near the blade root and tip sections. The outer boundaries of the grid were located at 0.9 R from the blade surfaces except in the span–wise direction where they were at 0.5 R from the blade tip and in the wake direction where they were located 1.2 R from the trailing edge.

4 Results and comparisons

Figure 8 show the comparison between experimental and numerical results for the non–dimensional vertical and longitudinal loads acting on the wing as function of C_T/σ. For the sake of clarity, both figures have been reported without the measurement uncertainty. The maximum values of the standard deviation of the non–dimensional vertical and longitudinal wing loads are respectively equal to 4×10^{-4} and 2×10^{-2}. The evaluation of the standard deviation has been carried out by taking into account the accuracy of the instruments as well as the measurement repeatability. The latter source of uncertainty has been evaluated over 40 measurement points acquired for the trim condition at $\theta = 12°$. As expected, the vertical force/thrust ratio being less than 1 % for all the C_T/σ tested. However, for C_T/σ greater than 0.058 the F_z^w/T is slightly positive (upload). The agreement between numerical calculations and experimental data is rather good in both cases demonstrating

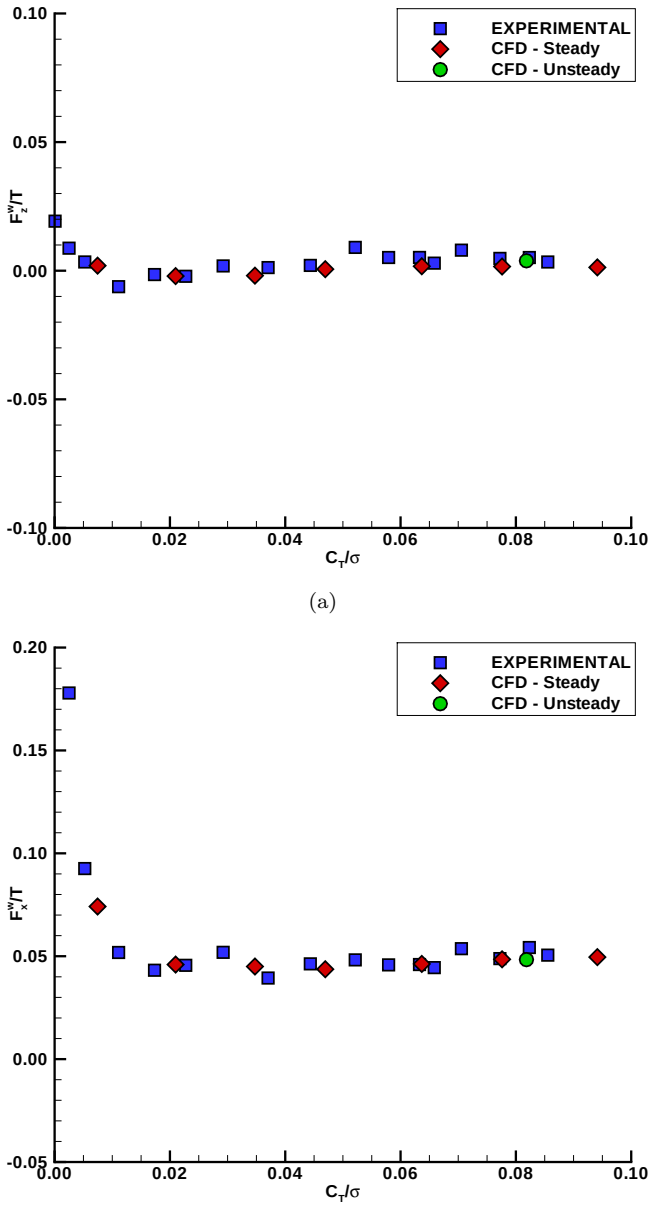

Figure 8: Comparison between experimental data and CFD calculations: a) F_z^w/T and b) F_x^w/T as function of C_T/σ, for $M_{Tip} = 0.32$.

that the CFD code ROSITA is capable to predict the global loads of the whole aircraft. However, for C_T/σ higher than 0.06, the values of the vertical force component F_z^w predicted by the CFD code are slightly lower with respect to the experimental data. An upload effect is still present but the predicted force/thrust ratio is less than 0.3 %.

The unsteady simulation has been carried out for the trim condition TC6 of the rotor ($\theta = 12°$, $\beta = 2.5°$) on a total of 10 rotor revolutions [29]. Every time step the blades and their grids were rotated of 2°. The master

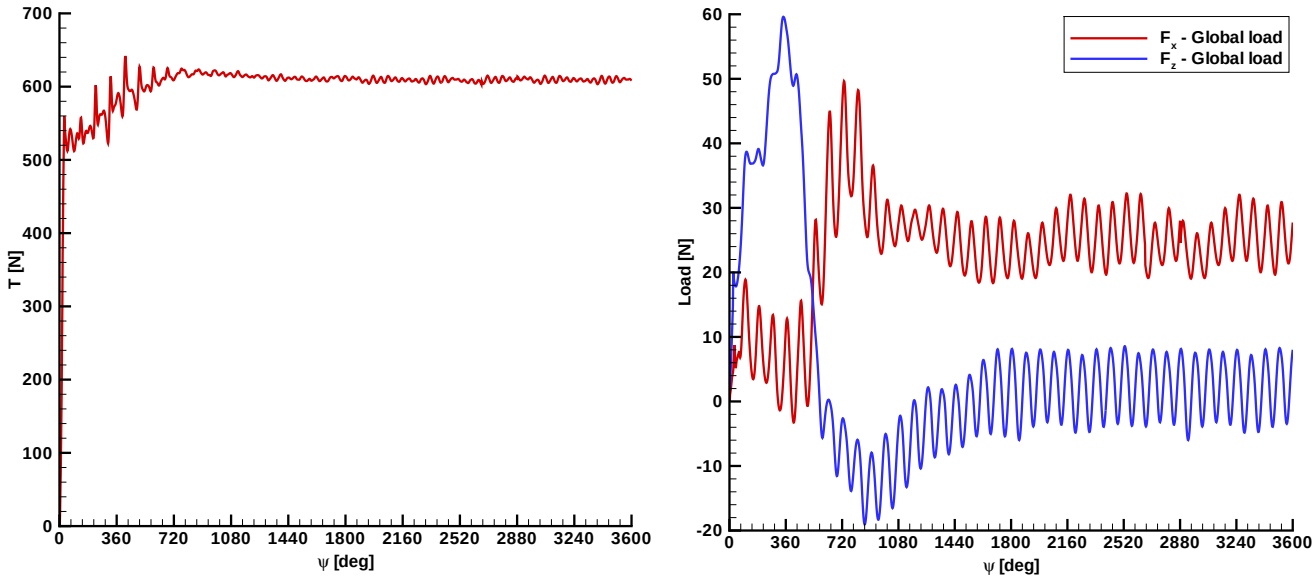

(a) (b)

Figure 9: Load time history from unsteady CFD calculations: a) rotor thrust T and b) wing global F_x^w and F_z^w.

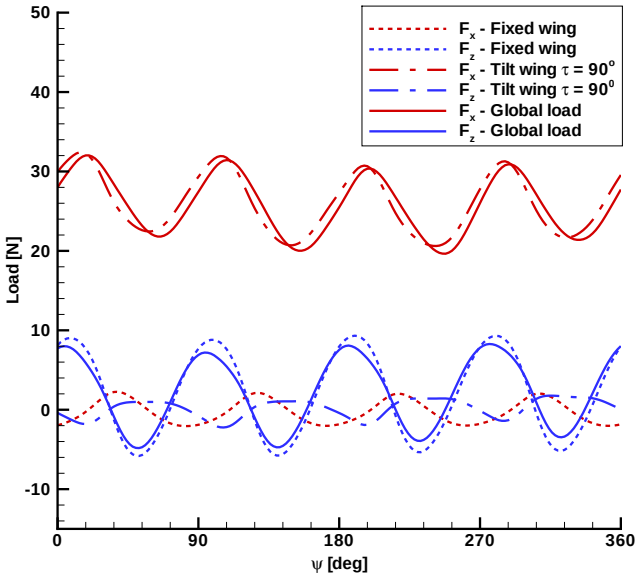

Figure 10: Wing loads (last rotor revolution).

blade (blade number 1) was considered in the blade reference position when its non–feathering axis is aligned with the wing rotational axis in the negative direction of the y–axis. The blade phase angle ψ (around the z–axis) was kept equal to 0° when the master blade is in the blade reference position. The same convention was used for PIV measurements. To start the unsteady simulation, an impulsive start has been used at the first time step and the rotor forces became nearly periodic after the fourth revolution, as shown in Figure 9(a) where the rotor thrust time history is reported. However, since the free stream velocity is zero in hovering, the rotor wake system needed more than four revolutions to reach a fully developed state. After 6 rotor revolutions the wing was fully immersed in the rotor wake and also wing forces became nearly periodic. After 8 revolutions the rotor wake has been convected sufficiently far downstream from the wing system and both the rotor and the wing loads reached a converged state, demonstrating however a dependence on the blade azimuthal position. Figure 9(b) illustrates the behaviour of wing vertical F_z^w and longitudinal F_x^w loads during the 10 revolutions. This result is confirmed by looking at the behaviour of the forces induced by the rotor wake system on the rotor itself and on the wing surfaces during the tenth revolution. In particular, the time history of the wing vertical and longitudinal loads in the last revolution are shown in Figure 10 and are expressed in terms of azimuthal blade angle ψ. In this picture, contributions given by each single part of the wing are compared with the global airloads acting on the wing system. The predicted behaviour of the forces on the wing surfaces exhibited the characteristic frequency of 4 cycles per revolution, typical of a four–bladed rotor. The wing global loads predicted by the unsteady calculation have been shown as function of C_T/σ in Figure 8 where they are also compared with experimental results and steady calculations. The values of F_x^w/T and F_z^w/T reported in these figures are the mean values of the corresponding force components calculated over the last rotor revolution. As shown in Figure 8, wing loads are well predicted by the unsteady CFD simulation. In the first case, the agreement between the present result

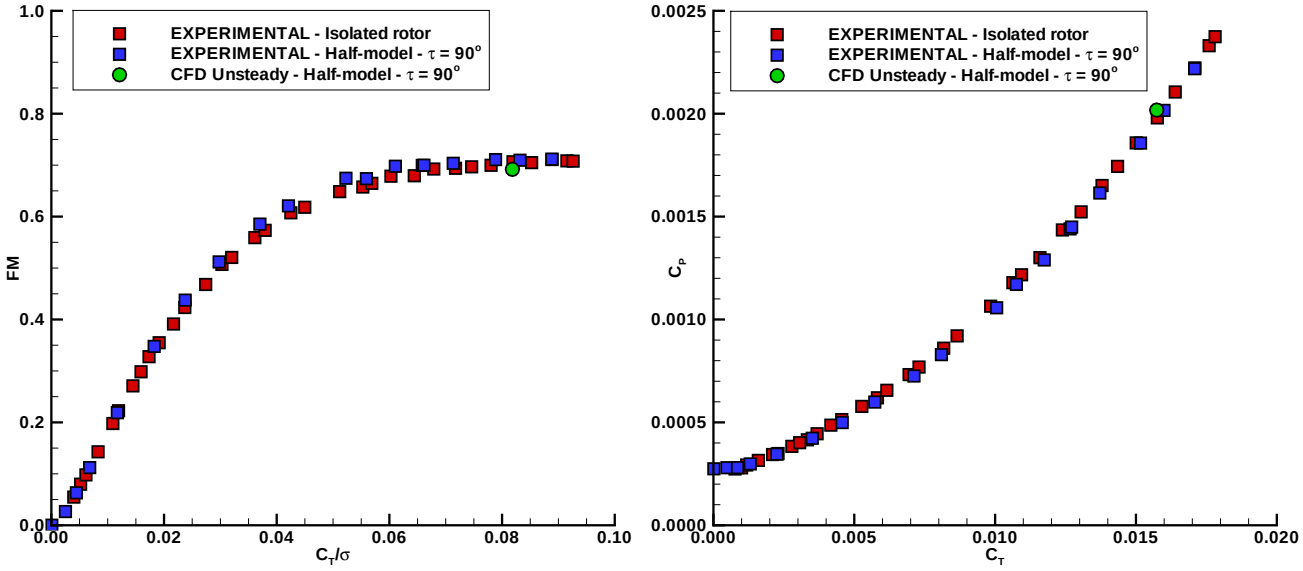

(a) (b)

Figure 11: Comparison between experimental data and unsteady CFD calculation: a) FM as function of $C_T\sigma$ and b) C_P as function of C_T, for $M_{Tip} = 0.32$.

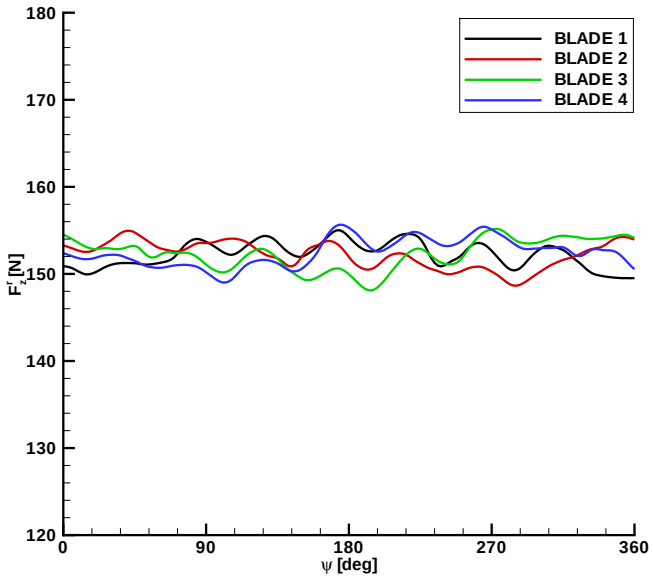

Figure 12: Rotor thrust (last rotor revolution).

and the experimental data is rather good and slightly better than in the steady case. On the other hand, the longitudinal force value F_x^w/T is almost equal to the steady results.

A rather good agreement with experimental data has been found also for rotor loads. The rotor hover performance are shown in Figure 11(a) and 11(b), detailing respectively the FM and power coefficient trends with thrust coefficient. In this case, the discrepancies between the numerical calculation and experimental data are mostly due to the fact that the rotor thrust and power are slightly overpredicted by ROSITA. Apart from that, the rather good agreement between experimental data and steady and unsteady CFD simulations confirm that ROSITA is capable to well predict the aircraft performance in hover in terms of global effects. In order to evaluate the effects of the wing system on the rotor performance, results for the half–model have been compared with the experimental results for the isolated rotor, as shown in Figure 11(a) and 11(b). In the latter configuration, the maximum value of the rotor FM achieved during the tests is 0.71 and it was obtained for $C_T = 0.0178$ and for $C_P = 0.0023$. Figure 11(a) and 11(b) demonstrate that minimising the wing surface on which the rotor wake strikes the rotor performance are very similar to the performance of the isolated hovering rotor. The influence of the wing on the rotor performance become substantially negligible if the portion of the wing immersed in the rotor wake system is rotated ($\tau = 90°$). More details about the effects of the wing configuration can be found in [10].

Even though the tilted wing is immersed in the rotor wake system, the load variations on the wing are more regular than the loads variation on the rotor blades, as demonstrated by comparing Figure 10 and Figure 12. This behaviour could be justified by looking at Figure 13 and 14, where the isolines of the vorticity vector modulus are plotted in correspondence of a plane passing through to the rotor axis and containing the wing rotational axis for two different blade phases (respectively $\psi = 45°$ and $\psi = 90°$). These figures suggest that

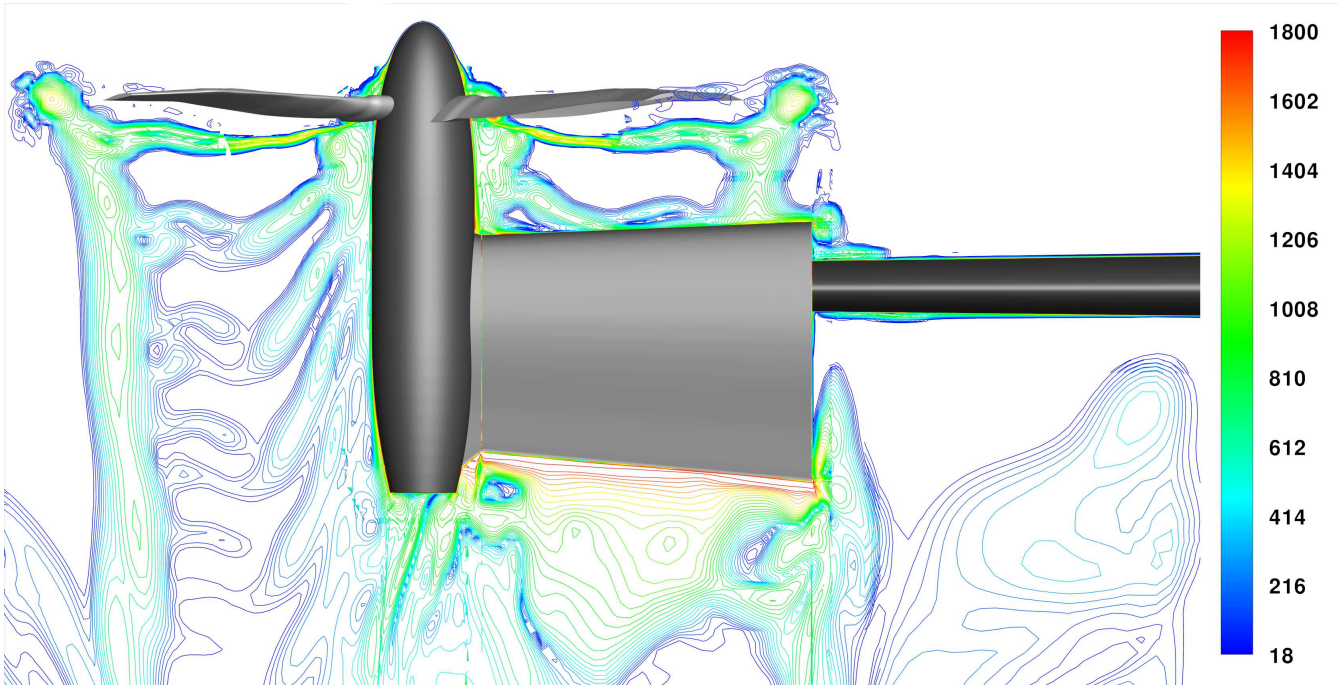

Figure 13: Unsteady vorticity magnitude contours for the tilted wing configuration at $\psi = 45°$, $M_{Tip} = 0.32$.

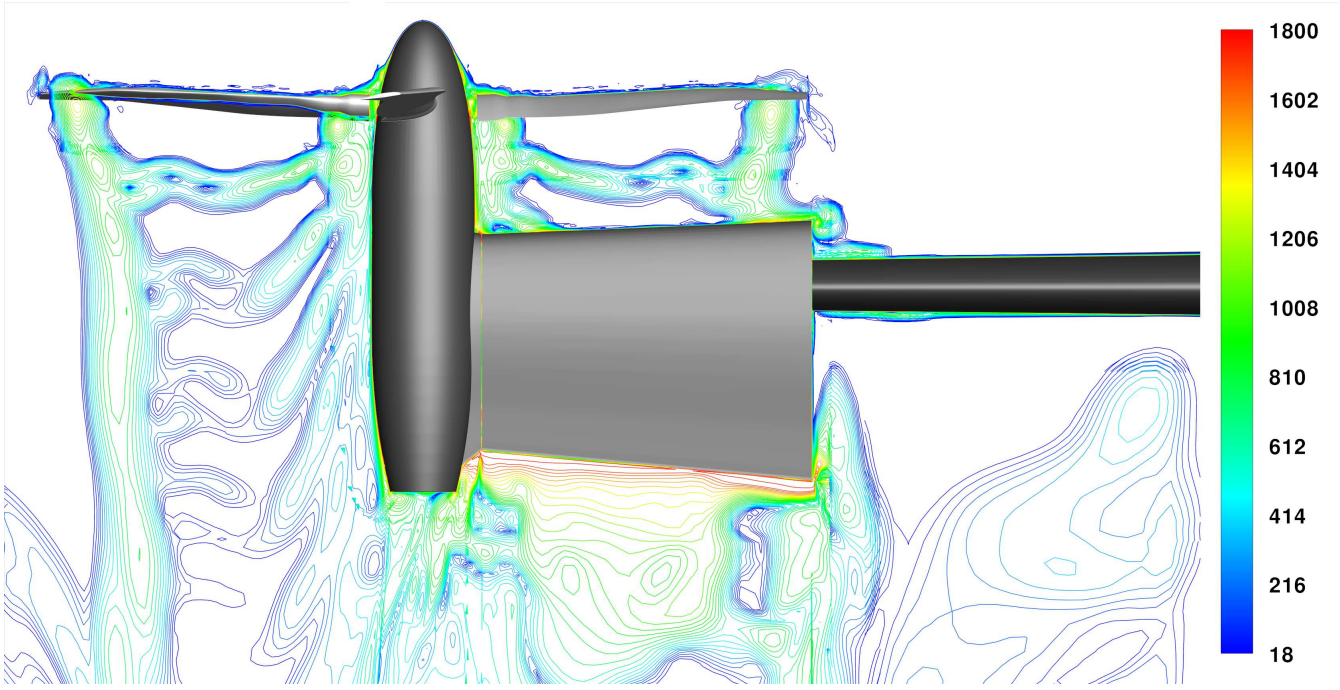

Figure 14: Unsteady vorticity magnitude contours for the tilted wing configuration at $\psi = 90°$, $M_{Tip} = 0.32$.

the wing system, and in particular the tilted wing portion, is subject to the forcing of rotor wake system that is almost periodic. Indeed, blade tip vortices are convected downstream from the rotor blades and strike on the leading edge of the tilted wing with a frequency of 4 cycles per revolution, as shown in Figure 10. On the other hand, the interaction which occur between a given blade and the tip vortex of the preceding one seems to be higher in the region above the wing with respect to other azimuthal blade positions. This phenomenon can be directly observed in Figure 12, where each blade vertical force F_z^r component is shown as function of the blade angle ψ. Each blade vertical load component exhibits a behaviour that is still periodic, but with a frequency of

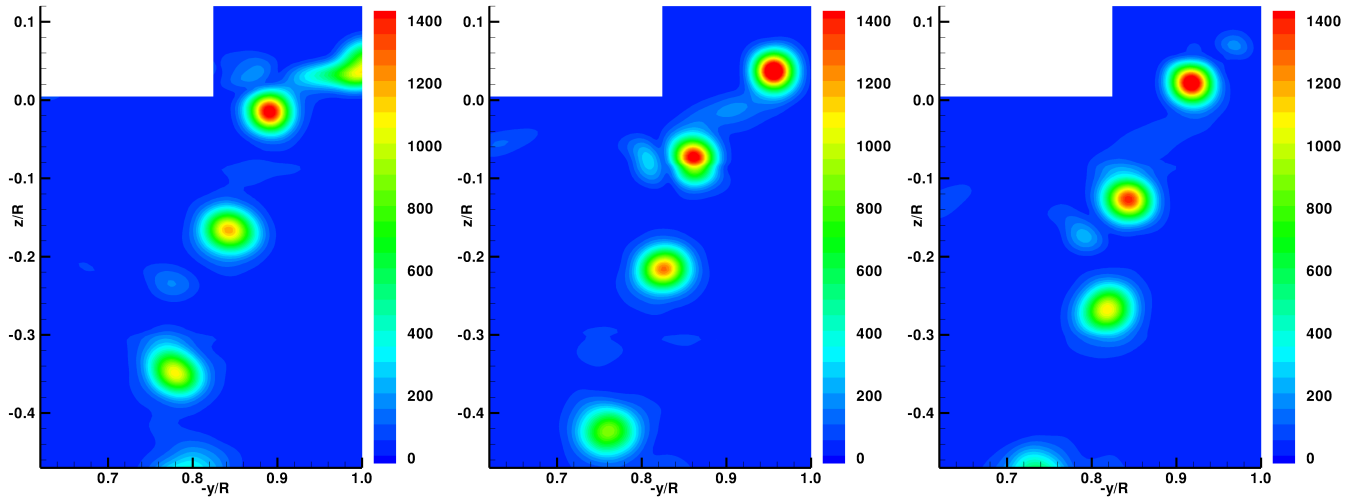

(a) Isolated rotor, $\psi = 15°$ (b) Isolated rotor, $\psi = 45°$ (c) Isolated rotor, $\psi = 75°$

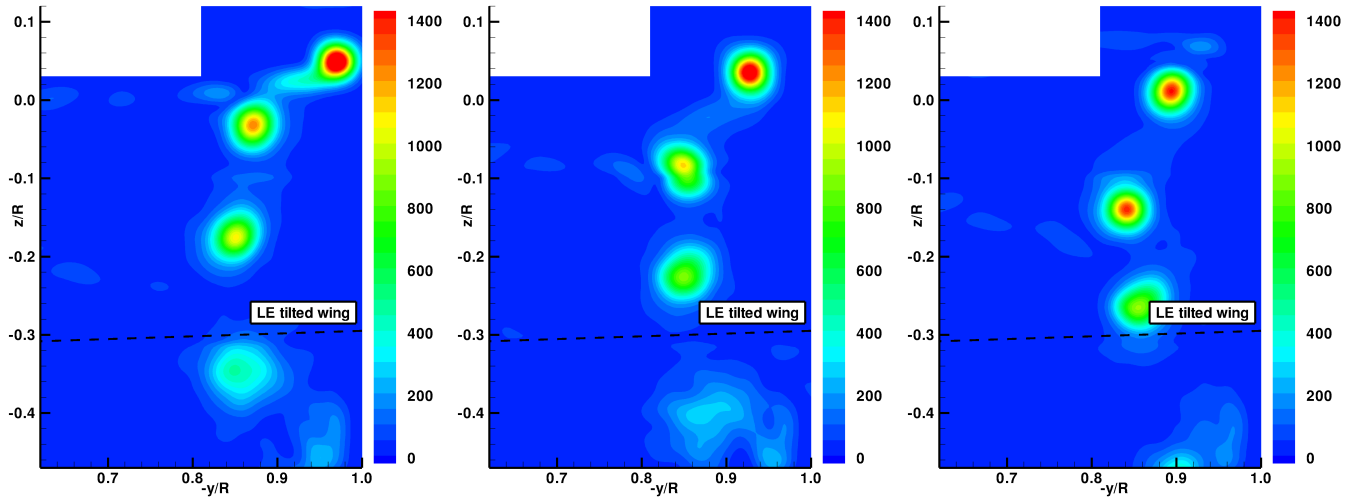

(d) Half–model, $\psi = 15°$ (e) Half–model, $\psi = 45°$ (f) Half–model, $\psi = 75°$

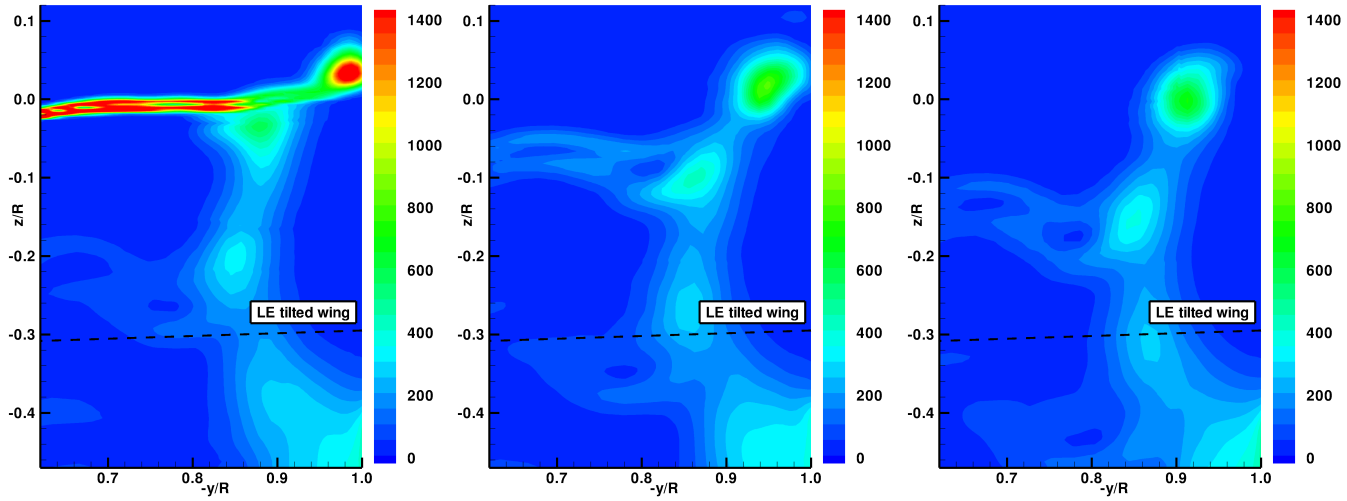

(g) Half–model, $\psi = 15°$ (h) Half–model, $\psi = 45°$ (i) Half–model, $\psi = 75°$

Figure 15: Vorticity contours $[1/s]$ comparisons: a–c) PIV data, plane $x/R = 0$ d–f) PIV data, plane $x/R = -0.079$ g–i) unsteady CFD calculation, plane $x/R = -0.079$.

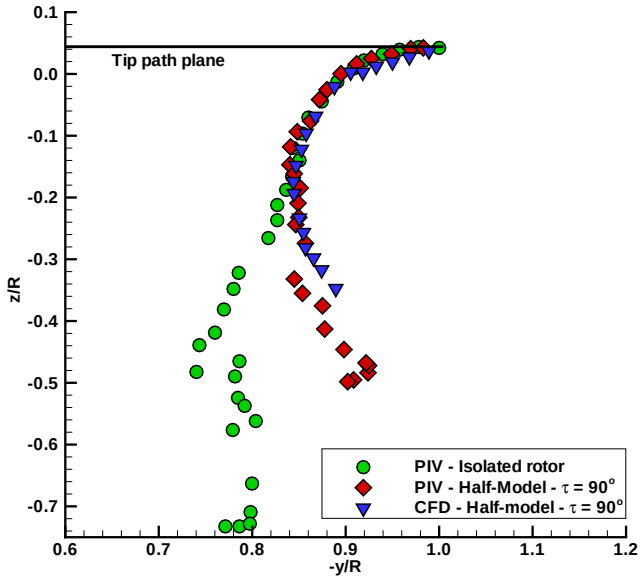

Figure 16: Tip vortex core displacements: comparison between PIV data (isolated rotor and half–model with tilted wing) and unsteady CFD calculation.

8 cycles per revolution.

In hovering the interaction between the rotor blade tip vortex structures and the tilted wing located below is responsible for the growth of unsteady phenomena that could have negative effects on the aircraft structure and dynamics. In order to describe how the wing modifies the rotor wake geometry, PIV surveys were carried out both on the isolated rotor and the half model with the external wing tilted ($\tau = 90°$). Figures from 15(a) to 15(c) show the phase–locked vorticity contours evaluated by PIV surveys in the wake flow below the isolated rotor for three different blade phases ($\psi = 15°$,45°,75°) in the x–constant plane shown in Figure 3(a). The evolution of the flow field in the rotor slipstream for further blade phases can be clearly observed, as well as the radial position of the tip vortex which moves progressively from the blade tip toward the rotor axis. The displacements of the blade tip vortex in the rotor wake, that are the regions where peaks of vorticity are present, were reported in Figure 16. The maximum contraction of the isolated rotor wake, which is 0.78 R, is reached at an axial distance from the rotor disk of $z/R = -0.4$. When the wing was placed below the rotor, the rotor wake system changed as confirmed by the PIV surveys on the half–model. Figures from 15(d) to 15(f) show the phase–locked vorticity contours measured in the x–constant plane shifted by $x = -0.079$ R with respect to the isolated case. In Figure 16 the tip vortex displacements of the rotor wake in the half–model configuration were also reported. In the half–model case it is apparent that when the rotor wake is approaching the tilted wing, the presence of the wing in the flow field prevents the natural wake contraction which assumes a minimum value of 0.85 R at $z/R = -0.14$.

PIV results for the half–model in the tilted wing configuration can be directly compared with the unsteady CFD simulation. Figures from 15(g) to 15(i) show the vorticity contours in the same plane of the PIV surveys for the same blade azimuthal positions. Even though the predicted location of the blade tip vortex is rather similar to the measured one, as shown also in Figure 16, its intensity is lower and decreases as the distance from the rotor disk increases. This effect is probably due to the high diffusion related to the grid elements dimension in that region. A much more intuitive comparison between numerical and experimental data is reported in Figure 17 where a three dimensional view of the iso–surfaces of the Q criteria around the half–model is given for the same blade phases of Figure 15(e), also shown in the figure. Despite the diffusion effects are present in the numerical simulation, Figure 17 demonstrates that the blade tip vortex path in the flow field region between the rotor disk and the wing leading edge is well predicted by ROSITA.

As already shown in Figure 8, the hovering aircraft in the tilted configuration experiences on the wing a very low vertical force together with a non–negligible longitudinal force. In this operating condition, the airloads which develop on the wing could be explained by the fact that the flow field below the rotor is characterised by a non negligible swirl component. PIV surveys in two y–constant planes ($y/R = -0.79$ and -0.69) near the wake rim were carried out to evaluate the x–velocity component U_x in the rotor wake over the leading edge of the tilted wing. Figure 18(a) and Figure 19(a) show the U_x velocity contours and the streamlines in the two measurement planes that were obtained by averaging acquired images for several blade phases. The streamlines within the rotor wake demonstrate that the flow strikes on the leading edge of the wing with a positive angle of attack with respect to the wing. Figure 18(b) and Figure 19(b) illustrate the same quantities in the same y–constant planes which were predicted by the unsteady CFD calculation. These images where obtained by averaging the flow field extracted in the last rotor revolution. Even though the comparison between CFD results and PIV data is rather good, in both planes the predicted flow field region near the upper part of leading edge of the sections shows higher positive values of U_x with respect to PIV. Figure 20 illustrates the U_x and U_z velocity profiles extracted in the vertical direction over the leading edge of the airfoil sections. Both CFD and PIV results prove the existence of a non–negligible swirl component in the rotor wake system.

5 Conclusions

This work deals with the investigation of the problem of the aerodynamic interaction between the rotor wake

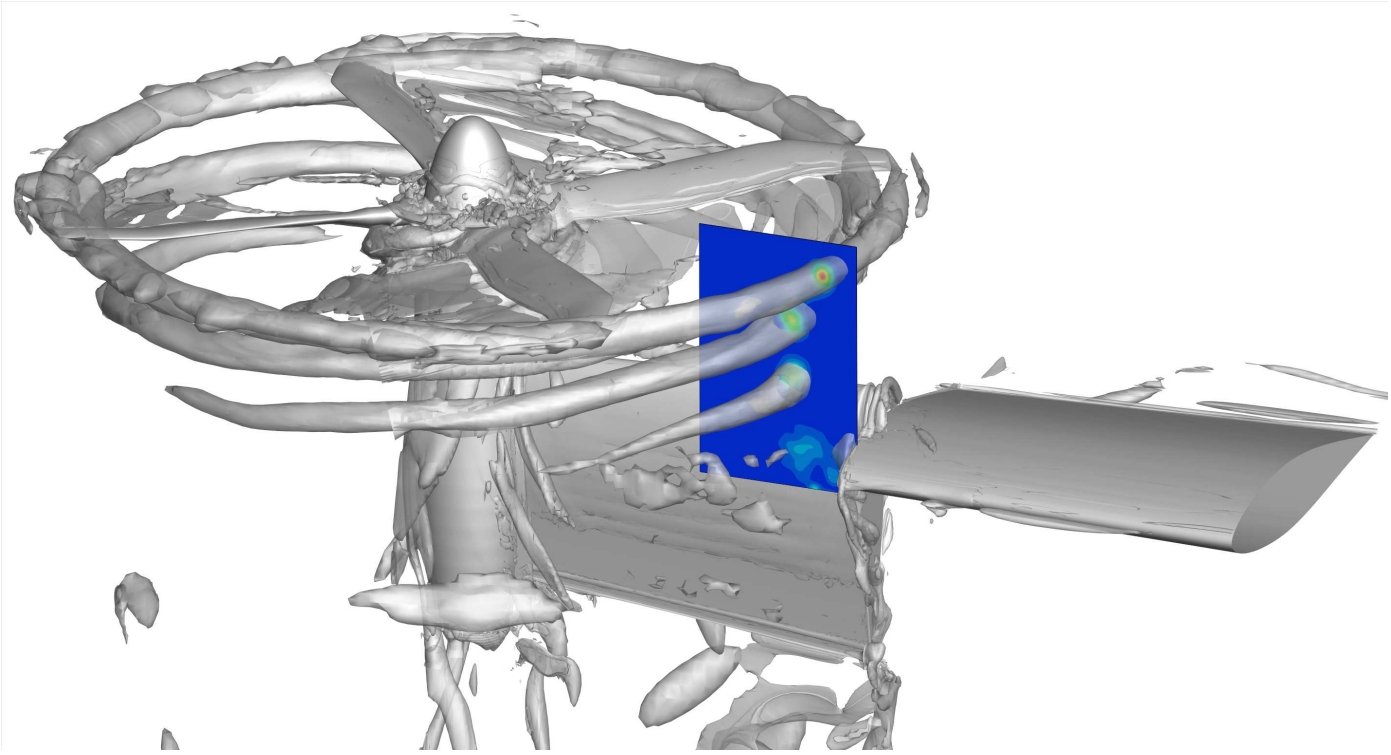

Figure 17: CFD visualisation of the Q criteria wake iso–surfaces ($Q = 3 \times 10^{-3}$, non–dimensional) and comparison with vorticity in the x–constant PIV plane at $\psi = 45°$.

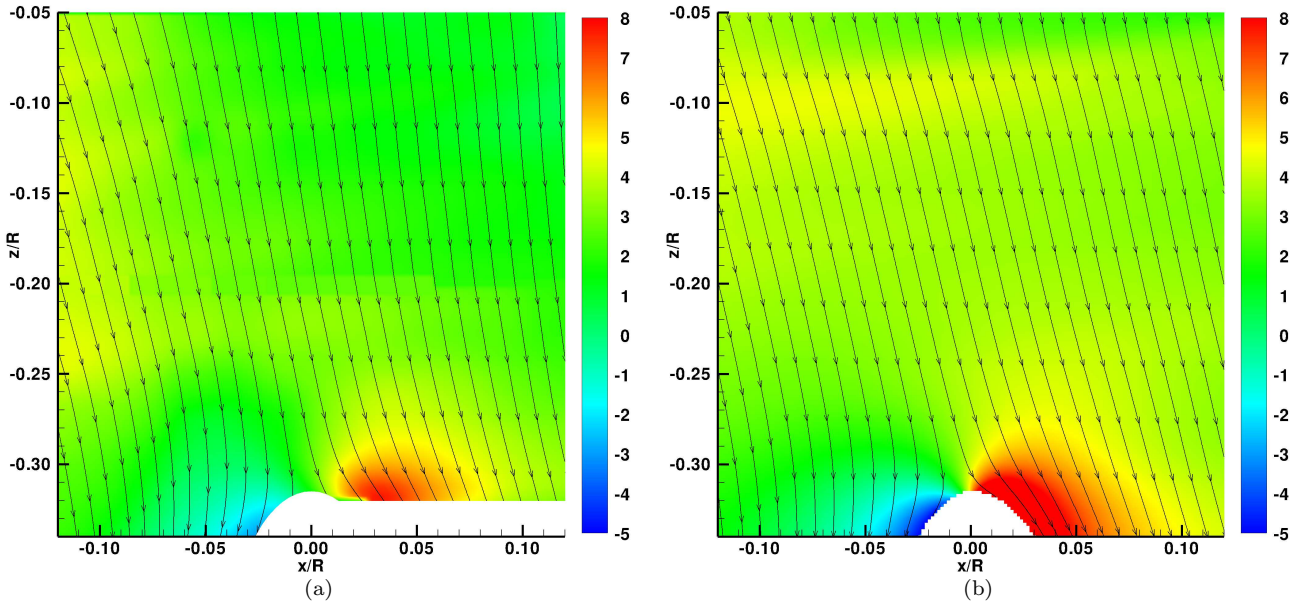

Figure 18: U_x velocity component contours [m/s] and in–plane streamlines in a plane at $y/R = -0.79$: a) PIV data and b) unsteady CFD calculation.

and the wing on a high–performance tiltwing aircraft which flies in hover. The interaction between the tip vortex structures generated from the rotor blade and the wing located below is responsible for the growth of unsteady phenomena that could have negative effects on the aircraft performance. With the aim to give a

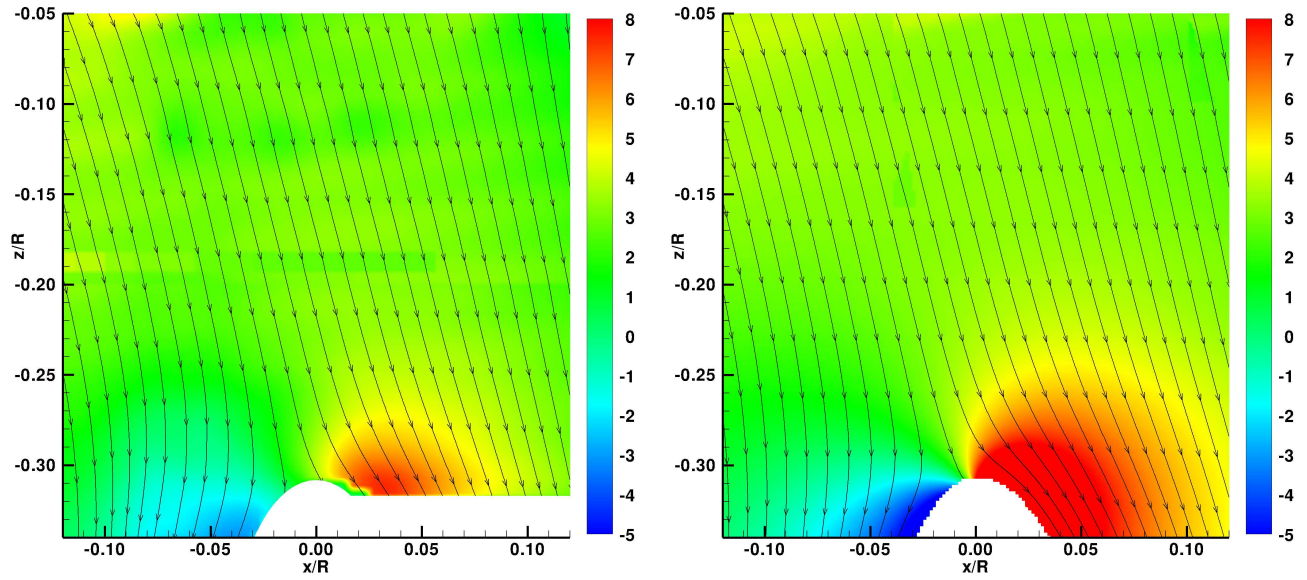

(a) (b)

Figure 19: U_x velocity component contours [m/s] and in–plane streamlines in a plane at $y/R = -0.69$: a) PIV data and b) unsteady CFD calculation.

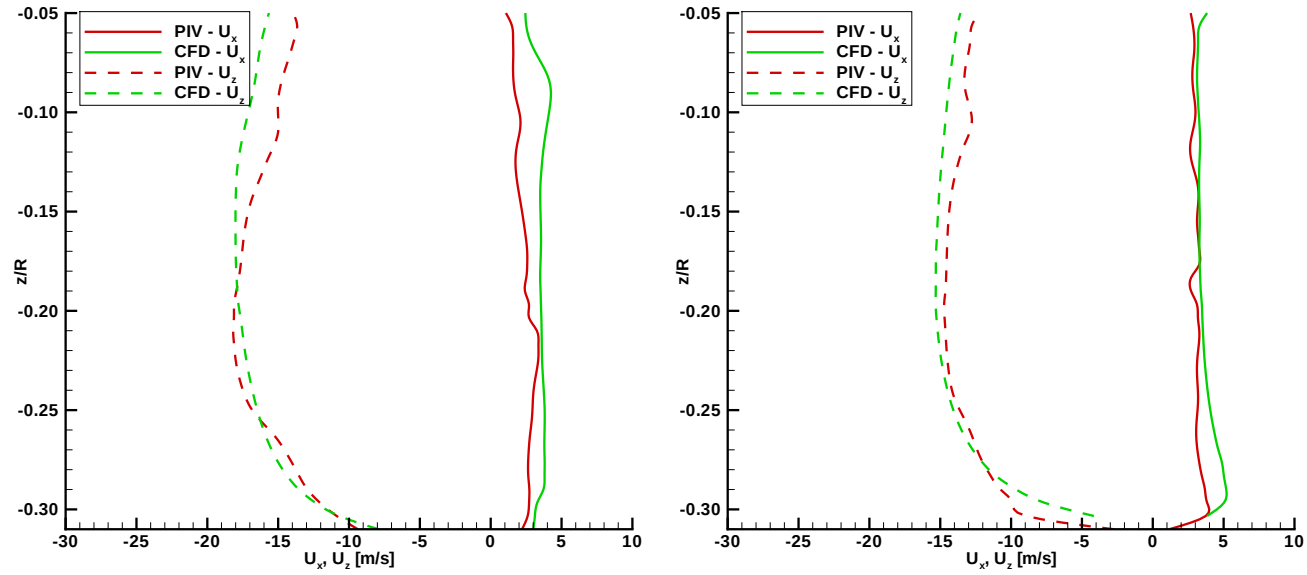

(a) (b)

Figure 20: Comparison between PIV data and unsteady CFD calculation, U_x and U_z velocity components: plane at a) $y/R = -0.79$ and b) $y/R = -0.69$.

detailed description of the main physical phenomena related to the wing–rotor interaction problem, a tiltwing aircraft has been analysed by means of both experimental and a numerical approaches. An experimental test rig representing one half of the aircraft has been manufactured at DAST Aerodynamic Laboratory of POLIMI and force and PIV measurement techniques has been adopted to study the aircraft performance and the flow field between the rotor and the wing. CFD simulations has been carried out making use of the in–house RANS code ROSITA. Several steady and one time accurate simulations have been carried out on the aircraft in the tilted wing configuration, showing a rather good agreement between numerical predictions and force and PIV data. Both experimental and numerical results demonstrated that rotor performance in the aircraft tilted wing

configuration were similar to the isolated rotor performance. Moreover, the capability to rotate the external part of the wing led in hover to an important reduction of the vertical force/thrust ratio that grows on the wing (less than 1 %). However, in the same flight condition the longitudinal force acting on the wing became non–negligible. Both PIV measurements and CFD calculations showed that the wing below the rotor significantly modified the flow field between the rotor disk and the tilted wing leading edge.

Copyright Statement

References

[1] Maisel, M., Giulianetti, D., and Dugan, D., "The history of the XV–15 tilt rotor research aircraft: from concept to flight," Monographs in Aerospace History, 17 SP–2000–4517, NASA History Division, Washington, D.C., USA, 2000.

[2] Reber, R., "Civil TiltRotor Transportation for the 21^{st} Century," *AIAA 93-4875*, AIAA International powered lift conference, 1993.

[3] Darabi, A., Stalker, A., McVeigh, M., and Wygnanski, I., "The Rotor Wake Above a Tiltrotor Airplane–Model in Hover," *AIAA*, 33^{rd} AIAA Fluid Dynamics Conference, Orlando, Florida, USA, 23–26 June 2003.

[4] Alli, P., Nannoni, F., and Cicalè, M., "ERICA: The european tiltrotor design and critical technology projects," *AIAA/ICAS*, International Air and Space Symposium and Exposition: The Next 100 Years, Day-ton, Ohio, USA, 14–17 July 2005.

[5] Droandi, G., Gibertini, G., and Biava, M., "Wing–Rotor Aerodynamic Interaction in Tiltrotor Aircraft," 38^{th} European Rotorcraft Forum, Amsterdam, The Netherlands, 4–7 September 2012.

[6] Droandi, G., Gibertini, G., Lanz, M., Campanardi, G., and Grassi, D., "Wing–Rotor Interaction On A 1/4–Scale Tiltrotor Half–Model," 39^{th} European Rotorcraft Forum, Moscow, Russia, 3–6 September 2013.

[7] Gibertini, G., Auteri, F., Campanardi, G., Macchi, C., Zanotti, A., and Stabellini, A., "Wind tunnel tests of a tilt–rotor aircraft," *The Aeronautical Journal*, Vol. 115, No. 1167, May 2011, pp. 315–322.

[8] Beaumier, P., Decours, J., and Lefebvre, T., "Aerodynamic and Aeroacoustic Desing of Moder Tilt–Rotors: the Onera Experience," *ICAS*, 26^{th} International Congress of the Aeronautical Sciences, Anchorage, Alaska, USA, 14–19 September 2008.

[9] Hakkaart, J., Stabellini, A., Verna, A., de Bruin, A., Langer, H.-J., Schneider, O., Przybilla, M., Philipsen, I., Ragazzi, A., and Hoejmakers, A., "First NICETRIP Powered Wind Tunnel Tests Successfully Completed in DNW-LLF," American Helicopter Society 70^{th} Annual Forum, Montreal, Canada, 20–22 May 2014.

[10] Droandi, G., Zanotti, A., Gibertini, G., Campanardi, G., and Grassi, D., "Experimental Investigation on a 1/4 Scaled Model of an High–Performance Tiltwing Aircraft in Hover," American Helicopter Society 70^{th} Annual Forum, Montreal, Canada, 20–22 May 2014.

[11] Droandi, G., *Wing–Rotor Aerodynamic Interaction in Tiltrotor Aircraft*, Ph.D. thesis, Politecnico di Milano, 2014.

[12] Droandi, G. and Gibertini, G., "Aerodynamic Blade Design With Multi-Objective Optimization For A Tiltrotor Aircraft," *Aircraft Engineering and Aerospace Technology*, 2014, in press.

[13] Abbott, I. and Doenhoff, A. V., *Theory of Wing Sections, Including a Summary of Airfoil Data*, McGraw–Hill Book Co., Inc. (Reprinted by Dover Publications, 1959), New York, 1949.

[14] L.K. Loftin, J., "Theoretical and Experimental Data for a Number of NACA 6A–Series Airfoil Section," Tech. Rep. TR–903 (Supersedes NACA TN–1368), NACA, 1948.

[15] Felker, F., "Wing Download Results from a Test of a 0.658-Scale V–22 Rotor and Wing," *Journal of the American Helicopter Society*, October 1992, pp. 58–63.

[16] Polak, D., Rehm, W., and George, A., "Effects of an Image Plane on the Tiltrotor Fountain Flow," *Journal of American Helicopter Society*, Vol. 45, No. 2, April 2000, pp. 90–96.

[17] Zanotti, A., Grassi, D., and Gibertini, G., "Experimental investigation of a trailing edge L-shaped tab on a pitching airfoil in deep dynamic stall conditions," *Proc of IMechE, Part G: Journal of Aerospace Engineering*.

[18] PIVTEC, "PIVview 2C version 3.0. User manual," `www.pivtec.com`, January 2009.

[19] Raffel, M., Willert, C., and Kompenhans, J., *Particle Image Velocimetry, a practical guide*, Springer, 1998.

[20] Biava, M., Pisoni, A., Saporiti, A., and Vigevano, L., "Efficient rotor aerodynamics predictions with an Euler method," 29^{th} European Rotorcraft Forum, Friedrichshafen, Germany, 16–18 September 2003.

[21] Spalart, P. and Allmaras, S., "One equation model for aerodynamic flows," *AIAA 92-0439*, 30^{th} AIAA Aerospace Science Meeting & Exhibit, Reno, Nevada, USA, 1992.

[22] Roe, P. L., "Approximate Riemann Solvers, Parameter Vectors and Difference Schemes," *Journal of Computational Physics*, Vol. 43, 1981, pp. 357–372.

[23] Venkatakrishnan, V., "On the accuracy of limiters and convergence to steady state solutions," *AIAA 1993–880*, 31^{st} AIAA Aerospace Science Meeting & Exhibit, Reno, Nevada, USA, 1993.

[24] Jameson, A., "Time Dependent Calculations Using Multigrid with Applications to Unsteady Flows past Airfoils and Wings," *AIAA 91–1596*, 10^{th} AIAA Computational Fluid Dynamics Conference, Honolulu, HI., 1991.

[25] Biava, M., *RANS computations of rotor/fuselage unsteady interactional aerodynamics*, Ph.D. thesis, Politecnico di Milano, Milano, Italy, 2007.

[26] Hirsch, C., *Numerical computation of internal and external flows*, John Wiley & Sons, 1988.

[27] Chesshire, G. and Henshaw, W. D., "Composite overlapping meshes for the solution of partial differential equations," *Journal of Computational Physics*, Vol. 90, 1990, pp. 1–64.

[28] Biava, M., Valentini, M., and Vigevano, L., "Trimmed Actuator Disk Modeling for Helicopter Rotor," 39^{th} European Rotorcraft Forum, Moscow, Russia, 3–6 September 2013.

[29] Potsdam, M. and Strawn, R., "CFD Simulations of Tiltrotor Configurations in Hover," *Journal of the American Helicopter Society*, Vol. 50, No. 1, 2005, pp. 82–94.